Polyamorphic Amorphous Silicon at High Pressure: Raman and Spatially Resolved X-ray Scattering and Molecular Dynamics Studies

Dominik Daisenberger,[†] Thierry Deschamps,[‡] Bernard Champagnon,[‡] Mohamed Mezouar,[§] Raúl Quesada Cabrera,[†] Mark Wilson,[||] and Paul F. McMillan*,[†]

[†]Department of Chemistry and Materials Chemistry Centre, Christopher Ingold Laboratory, University College London, 20 Gordon Street, London WC1H 0AJ, United Kingdom

[‡]Laboratoire de Physico-Chimie des Matériaux Luminescents, Université Claude Bernard Lyon 1, UMR 5620 CNRS, Université de Lyon, 12 rue Ada Byron, 69622 Villeurbanne cedex, France

[§]European Synchrotron Radiation Facility, BP 220, F-38043, Grenoble, France

[||]Department of Chemistry, Physical and Theoretical Chemistry Laboratory, University of Oxford, South Parks Road, Oxford OX1 3QZ

ABSTRACT: We studied the low-frequency Raman and X-ray scattering behavior of amorphous silicon (a-Si) at high pressure throughout the range where the density-driven polyamorphic transformation between the low-density amorphous (LDA) semiconductor and a novel metallic high-density amorphous (HDA) polyamorph occurs. The experimental data were analyzed with the aid of molecular dynamics (MD) simulations using the Stillinger—Weber potential. The heat capacity of a-Si obtained from the low pressure Raman data exhibits non Debye-like behavior, but the effect is small, and our data support the conclusion that no boson peak is present. The high-pressure Raman data show the presence of a distinct low frequency band for the HDA polyamorph in agreement with ab initio MD simulations. Spatially resolved synchrotron X-ray diffraction was used to study the high pressure behavior of the a-Si sample throughout the LDA—HDA transition range without interference by crystallization events. The X-ray data were analyzed using an iterative refinement strategy to extract real-space structural information. The appearance of the first diffraction peak (FDP) in the scattering function $S(Q)$ is discussed in terms of the void structure determined from Voronoi analysis of the MD simulation data.

Heat Capacity / T^3 Relation for Amorphous Si
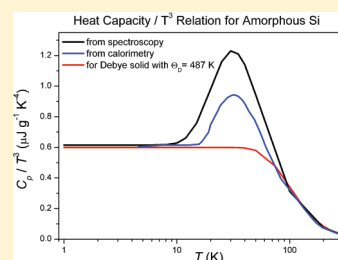
INTRODUCTION

Amorphous silicon (a-Si) is an important semiconducting material, and many studies have been devoted to understanding its structure and physical properties. It is well established that the structure is based on a random network of tetrahedrally bonded atoms.[1] The corresponding crystalline material has an indirect band gap at 1.4 eV accessible via phonon interactions: the first direct gap occurs in the UV region of the spectrum. Loss of translational symmetry in the amorphous solid leads to electronic excitation by light throughout the visible range, and this leads to the main application of a-Si in photovoltaic devices. The amorphous network contains a small proportion of broken bond defects that cause unwanted trapping of electrons, and these are usually passivated by incorporation of hydrogen to form a-Si:H materials. There have been many studies of the low temperature physics of pure and doped a-Si to understand the thermal properties, and particularly the excitations leading to non Debye-like behavior in the specific heat, $C(T)$.[2] At very low temperatures (e.g., $T < 10$ K), most amorphous solids exhibit a linear $C(T)$ dependence and an anomalous $T^{1.8}$ dependence of the thermal conductivity. These effects have been explained in terms of "two-level systems" (TLSs) related to various local defect models.[3−5] Such low energy excitations lead to unwanted noise and decoherence affecting the properties of low-temperature devices such as Josephson junctions and in quantum computing applications. However, such TLSs appear to be absent in a-Si, making it an ideal model material for study. At higher temperatures, in the 10−80 K range, amorphous materials typically exhibit a maximum in the C/T^3 function coupled with a plateau[3] observed in the thermal conductivity. These features are correlated with the presence of additional non-Debye-like excitations in the vibrational density of states (VDOS) between approximately 10−100 cm^{-1}, commonly referred to as the "boson peak". Models proposed for the appearance of the boson feature include the presence of nanoscale mechanical heterogeneities within the disordered structure that cause localization of acoustic modes along with additional excitations at the interfaces between "strong" versus "weak" regions (resulting in excess contributions to the VDOS at low frequency).[6] Other interpretations have been developed in terms of transverse acoustic (TA) phonons in glasses.[7] It has also been suggested that the existence of the boson peak could correlate with the "first (sharp) diffraction peak" (FDP or FSDP) observed in the structure factor, $S(Q)$, of amorphous materials, interpreted as

occurring due to nanoscale density fluctuations.[8−11] However, classic examples of amorphous solids including a-SiO$_2$, a-H$_2$O and a-Si appear to deviate from the general behavior, and both the presence of a boson peak and the interpretation of the first diffraction feature in $S(Q)$ have been questioned for these substances.[12−14] For a-Si, a maximum in the C/T^3 vs T function occurs near 30 K, but its magnitude is even smaller than that recorded for the corresponding crystalline material, which exhibits anomalous thermal expansion effects associated with phonon anharmonicity.[2,15]

In common with other tetrahedrally bonded amorphous solids including H$_2$O, GeO$_2$ and BeF$_2$, as well as a range of other substances, a-Si exhibits the unusual phenomenon known as "polyamorphism.[16−21] Under high pressure conditions, an abrupt transformation occurs between the tetrahedrally bonded amorphous semiconductor (the low-density amorphous state, LDA) and a new metallic high-density amorphous (HDA) form with the atoms in higher average coordination.[22,23] The polyamorphic transition has been studied by a range of experimental techniques and molecular dynamics (MD) as well as ab initio simulations, and it is thought to map on to a first-order phase transition occurring within the supercooled liquid state.[16,24−26]

In the present work we studied the low-frequency Raman spectrum of a-Si as a function of pressure throughout the range of the LDA−HDA transformation. From the (near) ambient pressure data we calculated the C/T^3 vs T relation for a-Si for comparison with data obtained by calorimetry. We also investigated the polyamorphic transformation by a new series of synchrotron X-ray microdiffraction measurements that allowed us to obtain spatially resolved data and study the behavior of the amorphous material to high pressure, free of contributions from Bragg scattering from metastably formed crystallites.[27] These data allowed a clear determination of $S(Q)$ to pressures above the LDA−HDA transition. Real space information was extracted from the X-ray scattering data by applying a self-consistent iterative refinement strategy.[28] We also investigated a-Si at high pressure by conducting MD simulations using a Stillinger−Weber (SW) potential.[23,27]

■ METHODS

Low-Frequency Raman Scattering at High Pressure. a-Si samples were prepared by chemical metathesis from the Zintl phase NaSi combined with NH$_4$Br.[29] The hydrogen content of these materials was shown to be minimal by IR absorption and neutron scattering studies. For Raman scattering experiments, powdered samples were pressed and loaded into a Boehler-Almax diamond anvil cell (DAC) using Re gaskets. Previous studies have indicated that the absence of a pressure-transmitting medium does not affect the interpretation of the high-pressure behavior. Pressure was determined via ruby fluorescence techniques for optical spectroscopy studies. Raman spectroscopy was carried out using a Dilor XY system with CCD detection using the 514.5 nm line of an Ar/Kr gas laser.[30,31] To record data within the low frequency region the premonochromator was adjusted to filter out elastic scattering contributions below 10 cm^{-1}, and the tilt of the sample chamber on the microscope stage was adjusted manually to minimize elastic scattering from both the incident laser beam at the top diamond surface as well as the diamond −sample interface. The series of sharp lines that appeared in the spectrum from the rotational excitations of N$_2$ and O$_2$ molecules in ambient air were then subtracted from the spectrum, along

with plasma lines arising from the incident laser beam. Remaining contributions from elastic scattering of the incident laser beam at the air−diamond and diamond−sample interfaces resulted in a steeply rising background below 10−20 cm^{-1}, and a further gently sloping background signal was observed due to weak luminescence of the a-Si samples toward the red end of the spectrum. These contributions were subtracted manually, or by applying standard curve shapes to model the background. During our experiments we could obtain spectra down to ∼30 cm^{-1} with minimal contributions from the exciting laser line at pressures up to 19 GPa, well above the LDA−HDA transformation pressure in the 12−14 GPa region.

The reduced Raman spectrum I^{red} is related to the Stokes Raman spectrum according to[32]

$$I^{red} = I^{Stokes} v \exp(\hbar v/kT)(v* - v)^{-4}$$

and the Raman active part of the VDOS is related to I^{red} according to

$$I^{red} = D(v)g(v)$$

Here v and $v*$ are the (absolute) Raman shift and the incident laser frequency respectively (both in Hz), $\hbar$ is Planck's constant over 2π, k is Boltzmann's constant, and $T = 300$ K. $g(v)$ is the VDOS, and $D(v)$ is a frequency- and polarization-dependent coupling parameter that has been determined experimentally for a-Si between 100 and 550 cm^{-1}.[33] Below 100 cm^{-1} and above 550 cm^{-1} for our studies, $D(v)$ was extrapolated from the measured values as being proportional to v^2 and v, respectively.[33,34]

For comparison with experimentally measured calorimetric data and to evaluate departures from Debye behavior, the heat capacity ($C_p \approx C_v$ at 300 K) was calculated from $g(v)$ according to harmonic theory:[35]

$$C_p(T) = 3R \int \frac{(hv/kT)^2 \exp(hv/kT)}{[\exp(hv/kT) - 1]^2} g(v) \, dv$$

where k again is Boltzmann's constant, h is Planck's constant, R is the universal gas constant, and $g(v)$ is in cm^{-1}.

X-ray Scattering. X-ray scattering experiments were carried out at beamline ID27 at the ESRF using angle-dispersive techniques with incident radiation $\lambda = 0.26472$ Å (46.8 keV). Amorphous scattering experiments require high reciprocal (Q) space coverage and accurate intensities to minimize errors when obtaining real space structural information by Fourier transformation.[28] Samples were loaded without any pressure medium or ruby chips into a Diacell-EasyLab membrane-driven DAC with opening angle 30° and X-ray transparent Be seats providing a maximum momentum transfer Q$_{max}$ = 9.6 Å^{-1}. The membrane pressure was calibrated beforehand in our laboratory at University College London against the ruby fluorescence scale to provide a reliable estimate of pressure in the sample chamber during the synchrotron X-ray diffraction run. Those experiments showed less than 1−2 GPa deviation in measured pressures across the sample chamber. We had previously carried out similar experiments at ESRF beamline ID-15-A where the incident beam size was 100 × 100 μm. Bragg contributions from some crystalline material that appeared in the sample under high pressure conditions had to be subtracted, and this resulted in some uncertainties in the data analysis.[27] Using the microdiffraction capability at ID27, the incident beam could be focused down to 2 × 3 μm and a matrix of spots throughout the sample was

14247

dx.doi.org/10.1021/jp205090s |J. Phys. Chem. B 2011, 115, 14246−14255

mapped at each pressure. This then allowed us to select those regions that were free from any crystalline contributions to study the a-Si behavior to the highest pressures possible.

To analyze the X-ray scattering data and extract $S(Q)$ background subtraction and data correction procedures were implemented following the methodology described by Eggert et al.[28] The measured X-ray intensity, $I^{\text{meas}}(Q)$, contains contributions from the sample and background:

$$I^{\text{meas}}(Q) = T(Q)I^{\text{samp}}(Q) + sI^{\text{bkgd}}(Q)$$

Here $I^{\text{bkgd}}(Q)$ is the measured DAC background, $T(Q)$ and s are the DAC transmission and background scale factors, respectively (s can vary due to fluctuations in beam intensity during the experiment). The DAC background scattering contribution was recorded by performing measurements with the DAC containing no sample but mounted in the beam with the same orientation and gasket as during experiments.

Introducing a normalization factor N, the total scattering from the sample, $I^{\text{samp}}(Q)$, is expressed as a sum of coherent, $I^{\text{coh}}(Q)$, and incoherent scattering, $I^{\text{incoh}}(Q)$

$$NI^{\text{samp}}(Q) = I^{\text{coh}}(Q) + I^{\text{incoh}}(Q)$$

The incoherent scattering contribution is computed analytically,[36] and N is determined by the Krogh−Moe−Norman expression:[37,38]

$$N = \frac{-2\pi^2\rho_0 Z^2 + \int_0^{Q_{\max}}([f^2(Q) + I^{\text{incoh}}(Q)]Q^2)\,\mathrm{d}Q}{\int_0^{Q_{\max}}(I^{\text{samp}}(Q))Q^2\,\mathrm{d}Q}$$

where ρ_0 is the average number density, Z is the atomic number, and $f(Q)$ is the atomic form factor. The structure factor is

$$S(Q) = \frac{1}{f^2(Q)}[NI^{\text{samp}}(Q) - I^{\text{incoh}}(Q)] = \frac{I^{\text{coh}}(Q)}{f^2(Q)}$$

and the real-space distribution function, $F(r)$, is the Fourier transform of $Q[S(Q) - 1]$:

$$F(r) = 4\pi r[\rho(r) - \rho_0] = \frac{2}{\pi}\int_0^{Q_{\max}} Q[S(Q) - 1]\sin(Qr)\,\mathrm{d}Q$$

Given a set of raw $I^{\text{meas}}(Q)$ and $I^{\text{bkgd}}(Q)$ scattering intensities, the only information required to obtain $S(Q)$ and hence $F(r)$ are the incoherent (Compton) scattering contribution, the atomic scattering factor, $T(Q)$, the number density, and the background scale factor. The Compton scattering contribution[36] and the atomic scattering factor[39,40] (both in electron units) are tabulated in the literature and/or can be calculated analytically. $T(Q)$ is constructed according to the downstream diamond anvil and backing plate geometries together with the mass absorption coefficients at the operating X-ray wavelength.[28,41]

The density (at high pressure) and the background scale factor are unknown quantities that must be determined in order to obtain $S(Q)$ and $F(r)$. The uncertainty in determining ρ_0 and s will introduce errors into the normalization, as both of these variables are needed to find N. Errors due to incorrect background subtraction will also be introduced due to the uncertainty in determining s. $S(Q)$ will also suffer from normalization errors due to the finite $Q_{\max}$ of the integrals in the expression for N. However, the effects of finite $Q_{\max}$ on $F(r)$ as obtained by Fourier transform of $Q[S(Q) - 1]$ are more substantial.[42,43]

Methods to account for normalization and background subtraction errors and to obtain better estimates of ρ_0 and s directly from the X-ray scattering data have been proposed.[28,42] It has been shown that s and N are independent, and errors in either introduce unphysical oscillations into $F(r)$, which are largest at low r and decay with r. As $F(r)$ must be equal to $-4\pi\rho_0 r$ before the nearest neighbor peak, these oscillations can be used as iterative feedback to obtain corrected values of $S(Q)$. This principle originally proposed by Kaplow et al.[42] was developed by Eggert et al.[28] into a self-consistent iterative refinement strategy to obtain better estimates of $S(Q)$ and $F(r)$ from DAC amorphous X-ray scattering experiments. According to Eggert et al. the difference between the experimentally determined $F(r)$ and its expected shape ($\Delta F(r)$) up to the base of the nearest neighbor peak ($r_{\min}$) is reverse Fourier transformed to obtain an improved estimate of $S(Q)$.

$$F_i(r) = \frac{2}{\pi}\int_0^{Q_{\max}} Q[S_i(Q) - 1]\sin(Qr)\,\mathrm{d}Q$$

$$\Delta F_i(r) = F_i(r) - (-4\pi r\rho_0)\ \text{for } r \text{ upto } r_{\min}$$

$$S_{(i+1)}(Q) = S_{(i)}(Q) - \frac{1}{Q}[S_{(i)}(Q)]\int_0^{r_{\min}}\Delta F_{(i)}(r)\sin(Qr)\,\mathrm{d}r$$

where i represents the number of iterations. The improved estimate of $S(Q)$ is then used to obtain an improved $F(r)$, and the whole process generally converges after a few iterations. Eggert et al. have also shown that this method can in fact be used to extract s and the density (and hence N) directly from the experimental data by minimizing $\Delta F(r)$ with respect to these two variables.[28] They define a χ^2 figure of merit

$$\chi^2_{(i)}(\rho_0, s) = \int_0^{r_{\min}}[\Delta F_{(i)}(r)]^2\,\mathrm{d}r$$

and according to their work there is a unique, well-defined minimum in $\chi^2_{(i)}$ for $i \leq 4$ at given $Q_{\max}$.

Although the iterative refinement strategy minimizes errors in s and N, it does not eliminate errors in $F(r)$ due to the finite $Q_{\max}$ employed when Fourier transforming $S(Q)$. The finite $Q_{\max}$ of the integrals in the expression for N will also introduce errors into $S(Q)$ and $F(r)$, but unless $Q_{\max}$ is very small, these effects will not be large and are probably (over) compensated for by the iterative refinement. Finite $Q_{\max}$ during Fourier transform introduces so-called termination ripples into $F(r)$, and no definite way has so far been found to overcome this problem. Windowing functions can be applied, but these significantly lower the resolution of the resulting real space data. A method often employed for DAC scattering data, which does not affect the resolution, is to plot $F(r)$ obtained from the same $S(Q)$ data terminated at different values of $Q_{\max}$. In this way, a range of $Q_{\max}$ over which the $F(r)$ data is self-consistent can be identified although the resulting data are still affected by termination ripples. Applying the same approach to the iterative refinement strategy shows that the values of density and s corresponding to minima in χ^2 also vary with $Q_{\max}$ and that there also is a range of $Q_{\max}$ over which the values are constant or at least self-consistent.[28]

All the experimental X-ray and real space data presented here were obtained using the iterative refinement strategy. All refinements converged after two iterations, and the real space data (and s and the density) were found to be self-consistent in the

Q_{max} range of 9 Å^{-1} to 9.6 Å^{-1}. All data are therefore plotted for every 0.2 Q_{max} in this range, giving the curves a certain thickness that is representative of the inherent uncertainty (Figure 6). In order to avoid reintroducing errors into the data set, we limited ourselves to only extracting the real-space distribution function $F(r)$, rather than deriving pair or radial distribution functions, that are further affected by the density. This allowed us to monitor the changes in the nearest and next nearest neighbor distances across the LDA–HDA transition, but we could not extract information on the changes in the coordination number. However, that information was available from the results of our MD simulations.

MD Simulations. We used an SW[44] potential to conduct isothermal–isobaric simulations of a-Si in parallel with our experimental investigation. Properties of a-Si networks simulated by the three most common potential models (Tersoff, EDIP, and SW) are generally similar.[45–47] Our choice of potential in this work allows a direct comparison with previous studies of the predicted low-density to high-density polyamorphic phase transition in liquid silicon.[23,27] It is well-known that rapidly cooling the SW liquid in MD simulations results in networks that do not reproduce the experimental a-Si radial distribution function and which are of too high density and mean coordination number.[1,48,49] To obtain a simulated a-Si network that is more representative of the experimental material, we followed the method of Luedtke and Landman[48] by increasing the weighting of the SW three-body term (which stabilizes tetrahedral bonding arrangements) during cooling from the liquid. The hence obtained zero pressure a-Si network has a density of 2.268 g cm^{-3} and mean coordination number of ∼4.1 (compared to 2.285 g cm^{-3} and ∼3.84, respectively, from experiment[1,49]) and is ∼86% four-coordinate with a narrow distribution of bond angles around 109.47°. The calculated structure factor and pair-distribution function agree well with those determined experimentally (Figures 6, 7). All subsequent (high pressure) simulations on this network were then conducted with the SW potential in its original form.

Simulations were conducted on a system of 216 atoms with periodic boundary conditions in a constant temperature and pressure (*NPT*) ensemble. Constant *P,T* conditions were maintained using Nosé–Hoover thermostats and barostats.[50,51] The time step employed was ∼0.5 fs and simulations were run for ∼120 ps at each pressure before ramping up in 1 GPa steps (beginning at zero pressure). The temperature was set at 300 K throughout. At each pressure the system volume and energy were monitored to confirm that they had relaxed sufficiently on the simulation time-scale. System properties were then calculated from the configurations generated over the second half of simulated time at each pressure. Real space distribution functions were calculated directly from the atomic coordinates, coordination numbers were calculated by setting the cutoff distance for a bond equal to the first minimum in the pair distribution function. Structure factors $S(Q)$ were obtained directly from the configurations according to

$$S(Q) = \langle A*(Q)A(Q) \rangle \text{ and } A(Q) = \frac{1}{\sqrt{N}} \sum_{j=1}^{N} \exp(iQr_j)$$

where r_j are the atom coordinates, Q is the wavevector, and the system has N atoms.

To calculate the VDOS, the Hessian (dynamical matrix) is calculated numerically and diagonalized.[52] The Raman-active spectrum of modes was then generated following the procedure
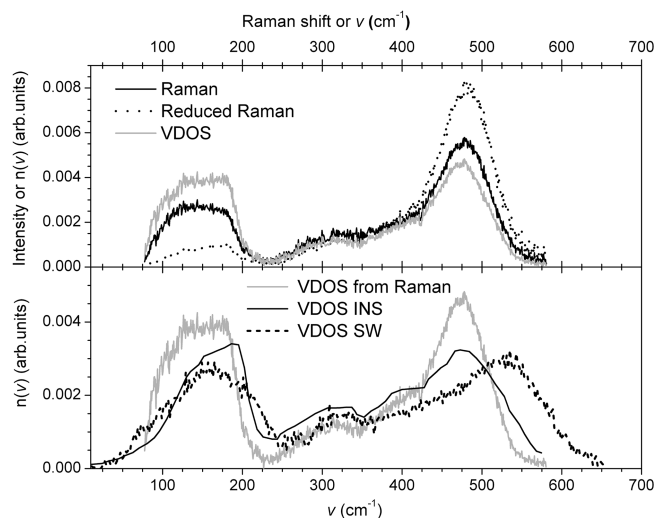

Figure 1. Top panel: a-Si Raman spectrum obtained at *P* = 0.8 GPa in the DAC, following baseline subtraction. Also shown are the reduced Raman spectrum and the VDOS obtained from the Raman data as described in the text. Bottom panel: VDOS of a-Si obtained from the Raman spectrum (as shown in the top panel) compared with the VDOS calculated from our SW MD simulation at zero pressure, and that obtained by INS.[59,62] The frequency (wavenumber) scale is identical in both panels and all curves are area normalized.

outlined by Vink et al.[53] The reduced Raman spectrum is related to the VDOS as described above. $D(\nu)$ expresses the light-vibronic coupling and contains the tensor $\alpha(\nu)$ calculated using a bond polarizability model.[54]

Void distributions were generated from the results of the MD simulations using a Voronoi construction in which space is subdivided into space-filling polyhedra.[55–57] The positions of the atom centers were used to generate the locations of the polyhedral centers (the Delaunay simplices). Each set of four atoms defines a void center (and an associated circumsphere) which is equidistant from those four atoms. The void structure was then analyzed by considering the distribution of the circumsphere radii. Additional spatial information was extracted by constructing pair distribution functions and structure factors from the circumsphere locations.

■ RESULTS AND DISCUSSION

The Raman spectrum obtained at near ambient conditions after loading into the DAC is shown in Figure 1, along with the reduced spectrum (I^{red}) and the VDOS obtained after application of $D(\nu)$. The spectrum is dominated by a strong band at 480 cm^{-1} along with a less intense broad feature centered at ∼150 cm^{-1}.[33,58] The strong high frequency band is due to transverse optic (TO) phonons associated with Si–Si stretching vibrations within the tetrahedrally bonded network.[52] Corresponding longitudinal (LO) contributions give rise to the low frequency shoulder commonly observed on this band. The weaker feature occurring near 300 cm^{-1} is usually interpreted as being due to tetrahedral bending modes, but it also contains contributions from acoustic overtones (e.g., 2TA) and combination (TO+TA) modes. At low frequency, the broad band occurring between 80 and 200 cm^{-1} is mainly assigned to TA vibrations, analogous to the VDOS determined for the corresponding crystalline material using inelastic neutron scattering

14249

dx.doi.org/10.1021/jp205090s |*J. Phys. Chem. B* 2011, 115, 14246–14255
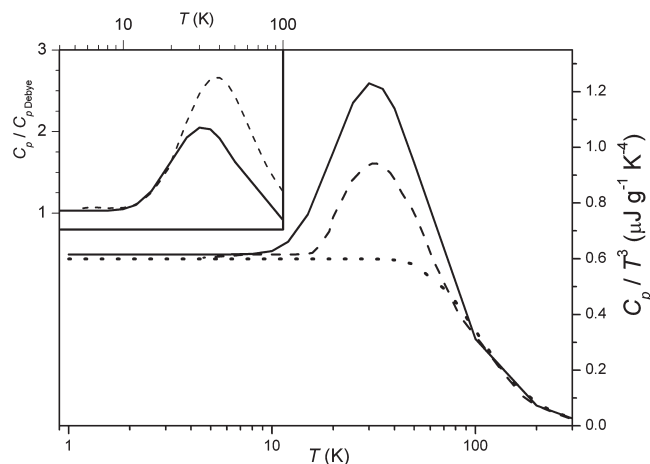
Figure 2. C_p/T^3 vs T relation for a-Si calculated from the VDOS obtained from the 0.8 GPa Raman spectrum (solid line), compared with the experimental results of Zink et al.[2] (dashed line) and the expected Debye behavior for $\Theta_D = 487$ K[2] (dotted line). Inset: C_p divided by the expected Debye behavior for a-Si (solid line) compared with crystalline Si (dotted line, data taken from Zink et al.[2]).


Figure 3. Raman spectra obtained for a-Si during compression in a DAC following baseline subtraction (see text). Successive data sets have been shifted upward along the y-axis for clarity. Pressures are indicated in GPa.

(INS) methods.[59] The reduced Raman spectrum has the same features occurring in similar positions but with modified relative intensities and with the TO maximum occurring at slightly higher wavenumber.[58,60,61] The VDOS obtained from I^{red} after application of the optical coupling parameter $D(\nu)$ shows TA and TO bands with nearly equal intensity, and both bands are also slightly broadened compared with the initial Raman spectrum.

The bottom panel of Figure 1 compares the VDOS obtained from our Raman experiments and that calculated from our zer-pressure a-Si SW MD simulations with the a-Si VDOS obtained in INS experiments.[59,62] The VDOS obtained from our Raman data (I^{red} and $D(\nu)$ treatment) is in reasonable agreement with that determined by INS, although the TA band is slightly shifted to lower frequency and is slightly more intense on its low wavenumber side. Apart from an almost systematic offset, the region between TA and TO bands maps well onto the INS VDOS. Both TA and TO bands appear slightly more intense in the VDOS obtained from I^{red}, and the TO/TA intensity ratio is >1, whereas it is <1 for the VDOS from INS. The TO band obtained by INS measurements is also slightly broader. Aside from a small intensity mismatch, the VDOS obtained from our SW MD simulations of a-Si matches very well with the INS VDOS up to about 350 cm^{-1}. As is well-known, the SW potential overestimates the frequency of the TO maximum,[63] but the band is very similar in shape to that of the INS VDOS and is of almost equal intensity.

From the VDOS obtained in our Raman experiments, the heat capacity function $C_p(T)$ was then evaluated to determine the C_p/T^3 vs T relation at low T in order to examine possible departures from Debye behavior. The C_p/T^3 vs T relation is plotted in Figure 2 together with the data from the direct C_p measurements of Zink et al.,[2] and compared with the expected behavior of a Debye-like solid, assuming a Debye temperature of 487 K.[2] Both the present data and the data of Zink et al. show a broad maximum in C_p/T^3 at $T \sim 31$ K. The C_p/T^3 relation obtained from our vibrational data shows a stronger excursion from the ideal relation between 10 and 100 K, with a maximum value that is about 30% higher. However, the two data sets are comparable.
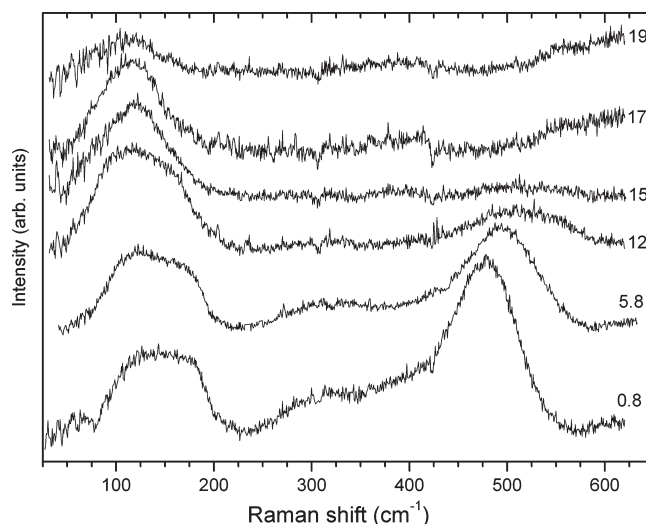
From Figure 2 it appears that both heat capacity determinations demonstrate a significant departure from the Debye relation in this range, and an initial conclusion might be that boson peak behavior is indeed present in a-Si.[2] However, the inset to Figure 2 shows C_p relative to the expected Debye behavior for crystalline silicon compared with a-Si. It can be seen that crystalline Si shows an even greater deviation from Debye behavior, with a large peak in C_p/T^3 vs T occurring at 38 K. This is attributed to anomalous thermal properties arising from anharmonic phonon contributions in the crystalline solid.[15] It has been concluded that there are in fact no "excess" low frequency modes in a-Si that would suggest a boson peak model for the amorphous material.[2] Instead, the maximum in the heat capacity can be understood in terms of the acoustic mode dispersion occurring within a mechanically homogeneous amorphous solid sample.[7]

During compression, the Raman data showed a rapid decrease in the intensity of the main Si–Si stretching peak accompanied by a marked broadening and loss of intensity (Figure 3). Above 15 GPa, only a very weak broad feature extending between approximately 300 and 450 cm^{-1} remained in this region of the spectrum above 15 GPa. These changes are consistent with the LDA–HDA polyamorphic transformation that produces a metallic high density form of a-Si.[21,23,64] Our earlier analysis indicated that the upper spinodal associated with the transition centered at approximately 9–10 GPa occurred at between 14 and 15 GPa. Our new data allowed us to track changes occurring in the low frequency part of the Raman spectrum.
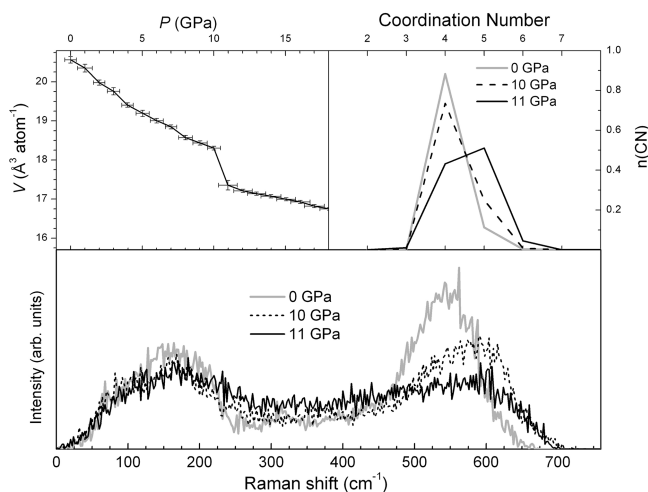
First, we clearly observe a distinct low frequency feature for both the LDA and HDA polyamorphs. As discussed previously, the band at low pressure exhibits a broad maximum between approximately 100 and 200 cm^{-1} and is associated with acoustic excitations in the amorphous solid. The bandwidth remains approximately constant with increasing pressure to about 12 GPa, but the relative intensity of the higher frequency component decreases slightly. We have plotted the average band position as a function of pressure in Figure 4. We observe a slight shift to lower wavenumber with increasing pressure. Interestingly, similar behavior is observed for crystalline silicon materials. In the case
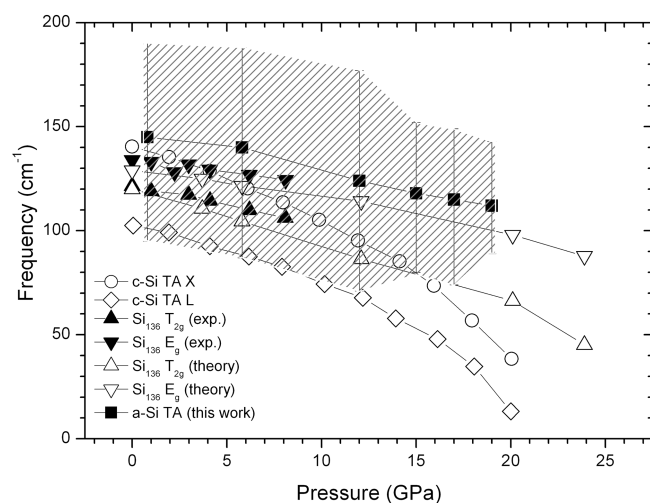
Figure 4. Frequency shift of the low frequency (TA) Raman band of a-Si with pressure. The solid squares indicate the approximate mean position of the broad band, and the upper and lower limits indicate the width at half-maximum. To highlight these data, the area between the lower and upper values is shown shaded on the diagram. The data are compared with DFT calculations of the TA mode of crystalline Si at the X and L points of the first Brillouin zone as a function of pressure,[65] and the T_{2g} and E_g zone center modes of silicon clathrate Si_{136}.[15,68]


Figure 5. Results of MD simulations. Top Left: Pressure—volume relations obtained in SW *NPT* simulations of a-Si. Top Right: Coordination number distributions within the simulated amorphous networks at zero pressure and at 10 GPa versus 11 GPa, just below and just above the predicted LDA—HDA transformation. Bottom: Raman spectra calculated from the simulated a-Si networks at 0, 10, and 11 GPa. The spectra represent an average over polarizability matrix elements to constitute a best estimate of the unpolarized spectra for comparison with experiment.

of diamond-structured Si and Ge, the TA phonons at the X and L points of the Brillouin zone soften with pressure and are expected to reach zero frequency above 20 GPa.[65,66] The predicted second-order phase transition is not achieved, however, as a first order transformation occurs into the metallic β-Sn structured polymorphs at 9—10 GPa. However, the atomic displacements required to transform the diamond structured materials into the β-Sn phase are similar.[65] For tetrahedrally bonded clathrate structures Si_{136} and Si_{46} that have been measured experimentally or predicted theoretically, a similar mode softening is observed for the lowest frequency Raman active T_{2g} and E_g modes (Figure 4), that can be related to acoustic-like modes within the folded Brillouin zone.[15,67−69] Experimentally, the Si_{136} clathrate transforms via a metastable first-order transition at 9—10 GPa into the β-Sn structured material.[70] Above 15 GPa, the low frequency band of the HDA polyamorph is significantly narrower and is more symmetric than the LDA feature (Figure 3, 4). This band is predicted both by our SW MD simulations of the VDOS and Raman spectrum (Figure 1, 5), as well as by ab initio simulation studies.[22] Interestingly, the low frequency band for the HDA polyamorph also decreases in frequency with increasing pressure, at a similar rate as that for the LDA form.

In Figure 5 we show the pressure—volume data obtained from our *NPT* SW simulations of a-Si and the coordination number (CN) distribution for three selected pressures. As the pressure is increased stepwise to 10 GPa, the network densifies continuously followed by a much larger jump in density between 10 and 11 GPa.[27] The coordination number distribution shows that the zero pressure network is dominated by four coordinate sites with a small number of five coordinate defects (mean CN ∼4.1). At 10 GPa, the network is still dominated by four coordinate sites, but the number of five coordinate defects has increased slightly (mean CN ∼4.3). The jump in density between 10 and 11 GPa is accompanied by a substantial increase in mean coordination number (to ∼4.6) as five coordinate sites now dominate and a few six- (and three-) coordinate sites have also now formed.

In the bottom panel of Figure 5 we show the Raman spectra calculated for the simulated a-Si networks at 0, 10, and 11 GPa. The calculated Raman spectrum at zero pressure agrees very well with the (near) ambient experimental data, although the frequency of the TO band is slightly overestimated, as expected.[63] As the pressure is increased, the calculated spectra show qualitatively similar changes to those observed in experiment. Initially, the TO band gradually shifts to higher wavenumber, loses intensity, and becomes wider. Between 10 and 11 GPa (where the jump in density to the HDA network occurs), the TA band becomes the most intense feature, and the TO band is now very wide and only slightly more intense than the region of the spectrum between 250 and 450 cm^{-1}. These changes in the Raman spectra can be associated with the substantial increase in the number of five coordinate sites.

The X-ray structure factors, $S(Q)$, obtained in our DAC compression experiments at ID27 are plotted in Figure 6, together with $S(Q)$ calculated from the simulated networks at 0, 10, and 11 GPa. At ambient pressure, $S(Q)$ of a-Si is dominated by a second diffraction peak (SDP) at 3.62 Å^{-1} and a less intense first diffraction peak (FDP) at 2.05 Å^{-1}.[1,43] $S(Q)$ calculated from the zero-pressure SW a-Si network is very similar in form to that obtained from experiment. As the pressure is increased, we observe similar changes in the experimental $S(Q)$ as reported previously.[27] In the present work, use of the focused X-ray beam allowed us to select regions of the sample that were free from microcrystallites at high pressure. Up to 13 GPa, the FDP shifts gradually to higher Q, whereas the position of the SDP remains almost constant. The intensities of the FDP and SDP also become more similar. Between 13 and 17 GPa, within the LDA—HDA transformation range, the FDP jumps to higher Q and increases in intensity relative to the SDP. These changes are mirrored in the simulation results. Up to 10 GPa, the FDP gradually moves to higher Q and gains in intensity, and the SDP also moves to slightly higher Q. Between 10 and 11 GPa, the FDP shifts substantially to higher Q and gains in intensity relative to
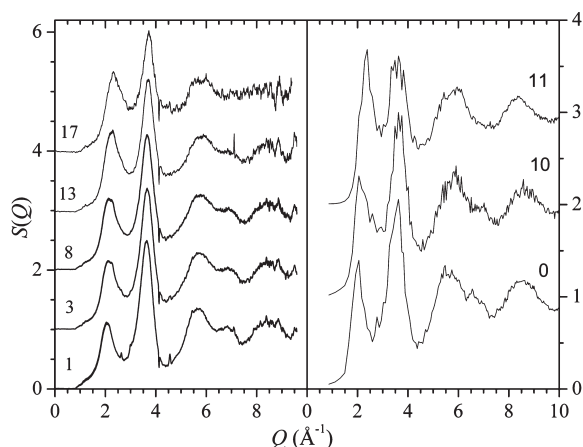
Figure 6. Experimental versus simulated X-ray scattering data. Left: $S(Q)$ obtained by experiment at ESRF ID27 during compression in a DAC. Successive data sets have been shifted upward by one unit each along the y-axis for clarity. Pressures are indicated in GPa. Right: $S(Q)$ calculated for the simulated a-Si networks at $P = 0$, 10, and 11 GPa. Successive data have been shifted upward by one unit each along the y-axis. Pressures are indicated in GPa.
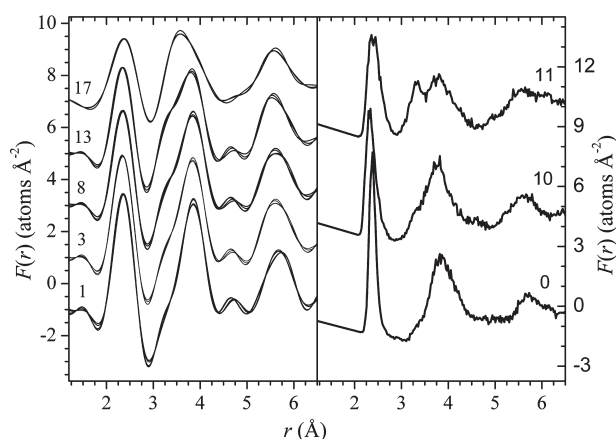

Figure 7. Comparison of $F(r)$ obtained by Fourier transform of the experimental $S(Q)$ (left, successive data have been shifted by 2 units along the y-axis) and directly from the atomic coordinates of the SW simulated a-Si networks (right, successive data have been shifted 5 units along the y-axis). Pressures in GPa are indicated in left and right panels.

the SDP to become the most dominant feature in the scattering function.

In Figure 7 we compare the $F(r)$ functions obtained by Fourier transformation from the experimental data (Figure 6) with those obtained directly from the atomic coordinates of the SW a-Si networks at $P = 0$, 10, and 11 GPa. As the pressure is increased to 13 GPa for the experimental data, the nearest neighbor feature moves slightly to lower r values. The low r side of the next-nearest neighbor feature also gains in intensity and has become a distinct shoulder by 13 GPa. Between 13 and 17 GPa the nearest neighbor feature shifts to higher r, and the maximum of the next-nearest neighbor feature moves to lower r. Again these changes are mirrored in the simulation results. Up to 10 GPa, the nearest neighbor feature moves to lower r, loses intensity, and becomes slightly broadened, consistent with a system densification arising from the contraction of the nearest-neighbor bond
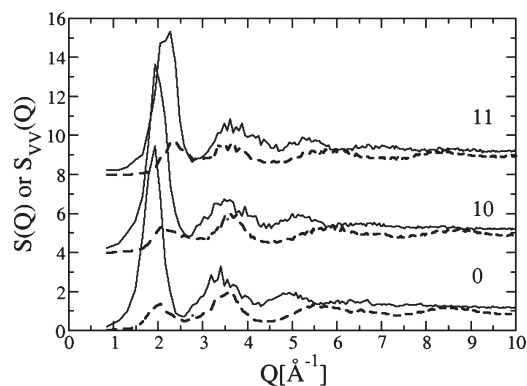
Figure 8. Atom—atom and void—void structure factors ($S(Q)$ and $S_{VV}(Q)$, dashed and solid lines, respectively) determined from the simulations at the three pressures indicated. The void—void function shows a stronger signal in the FDP and the shift to higher Q with pressure is mirrored in both functions. Successive functions are shifted along the ordinate axis for clarity.
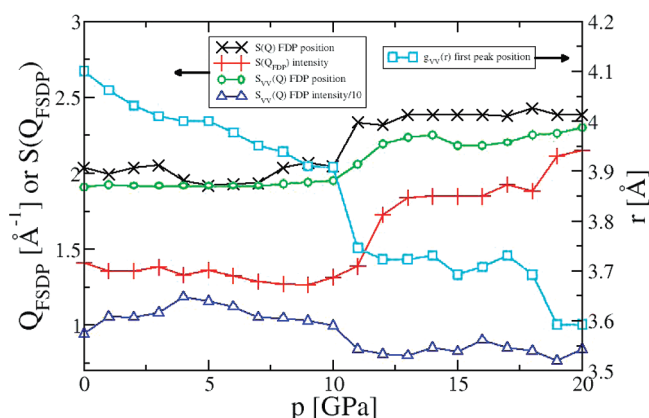
Figure 9. Key peak position and intensity changes as a function of pressure obtained from the present simulations. The $\times$ and $\bigcirc$ symbols show the change in position of the FDP in $S(Q)$ and $S_{VV}(Q)$, respectively. The $+$ and $\triangle$ symbols show the changes in intensity of the same two functions (the latter was divided by 10 to aid comparison). The $\square$ symbol shows the change in the position of the first peak in $g_{VV}(r)$ and refers to the right-hand ordinate axis.

lengths (while retaining the dominant four-coordinate atom motifs). The next-nearest neighbor feature also develops a distinct shoulder on the low r side at ~3.3 Å arising from the presence of significant edge-sharing of the higher coordinate species. At around 10—11 GPa, the nearest neighbor feature moves to higher r, loses intensity, and becomes broader, consistent with densification resulting from an increase in nearest-neighbor coordination number. The next-nearest neighbor peak develops a second maximum on its low r side.

We used our simulation results to examine how features in the $S(Q)$ scattering function such as the FDP might be correlated with the distribution of voids in the amorphous structure.[71] Figure 8 shows the void—void structure factors, $S_{VV}(Q)$ as a function of pressure compared to the corresponding atomic functions computed from our MD simulations. $S_{VV}(Q)$ shows significantly greater FDP intensity compared with the corresponding atomic functions. Figure 9 shows the dependence of the peak positions and intensities of both $S_{VV}(Q)$ and $S(Q)$ as a

14252

dx.doi.org/10.1021/jp205090s |*J. Phys. Chem. B* 2011, 115, 14246–14255
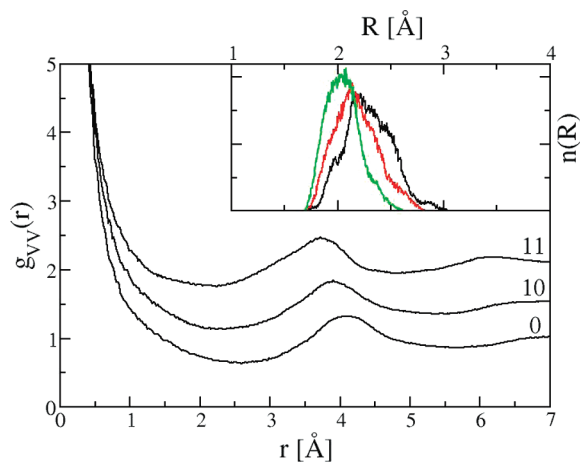
Figure 10. The main panel shows the pressure evolution of the void—void pair distribution function $g_{VV}(r)$. The functions obtained at the three pressures indicated are shown. The inset shows the respective circumsphere radii distributions with the black, red, and green lines showing the radii distributions at pressures of 0, 10, and 11 GPa, respectively.

function of pressure. The positions of the FDP in the two functions follows the same pattern as a function of pressure showing a shift to higher Q at $P \sim 10-11$ GPa. The intensity changes show different behavior with the FDP in $S(Q)$ increasing in intensity with increasing pressure, while the corresponding peak in $S_{VV}(Q)$ decreases. The intensity of the FDP is greater in $S_{VV}(Q)$ than in $S(Q)$ (as observed previously in network-forming molten salts[71]), which is simply related to the larger density of circumspheres associated with the larger voids. On pressurization, the system changes from a relatively open four-coordinate-dominated network structure (with accompanying relatively strong FDP signals in both $S(Q)$ and $S_{VV}(Q)$) to a more dense five-coordinate-dominated system in which the "additional" fifth atom now partially occupies the voids present at the lower densities and hence leads to both a shift (to higher Q) in both $S(Q)$ and $S_{VV}(Q)$ and a loss of intensity in $S_{VV}(Q)$. Figure 10 shows the real space void—void pair distribution functions, $g_{VV}(r)$, along with the circumsphere radii distributions (inset) as a function of pressure. On pressurization, the network void structure effectively collapses, resulting in a narrower distribution of smaller circumspheres (that is, a more regular void structure). This change is accompanied by a shift in the first peak in $g_{VV}(r)$ to lower r. This peak position is highly sensitive to the LDA—HDA transition (Figure 9).

The combined experimental and theoretical data presented here therefore strongly suggest that the structure of HDA-Si is that of highly defective tetrahedral network with mean CN ~ 5, in which the fifth neighboring atom occupies an interstitial position (a former void) of a distorted tetrahedron. From previous ab initio simulation studies, two significantly different HDA-Si networks have been suggested to exist following a polyamorphic transition at high pressure. Morishita[22] reported an HDA material with mean coordination number 5.1 that was only $\sim 10\%$ denser than LDA-Si. The changes in density and coordination environment across this LDA—HDA transition are very similar to our findings using the SW potential.[23,27] The VDOS of Morishita's network exhibited a distinct TA feature centered near 120 cm^{-1}, similar to that in the HDA spectra presented here (Figure 3). In contrast, Durandurdu et al.[72,73] observed a density-driven

transformation from LDA-Si into a high-density a-Si network with a mean coordination number of 8.6—9.2 that was $\sim 20\%$ denser than LDA-Si. Interestingly, the VDOS of Durandurdu et al.'s HDA network contained no distinct TA feature but instead showed a very broad, flat envelope of bands extending throughout the 100—550 cm^{-1} region.[72,73] The similarity of the present HDA Raman spectra to both the VDOS of the simulated SW HDA network and to that of Morishita's HDA network therefore strongly suggest that the structure of experimentally observed HDA-Si is that of a distorted, five-coordinate tetrahedral network rather than that of the higher density network reported by Durandurdu et al. The changes in density and coordination environment across the LDA—HDA transition also mirrors those between the low-density and high-density liquid (LDL and HDL) configurations sampled by the supercooled SW liquid at zero pressure.[22,23] This lends further support to the idea that the polyamorphic transition between LDA and HDA silicon maps onto a first-order transition between LDL and HDL silicon in the supercooled state.[16,24]

Regarding the experimental and theoretical X-ray data a further point to consider is whether the FDP is a FSDP, a feature often observed in both liquid and glassy system structure factors, or simply a principal peak, albeit at a relatively low scattering angle. In the present work the ambient pressure location of the FDP is at $Q \sim 2.05$ Å^{-1}, corresponding to density fluctuations on the order of ~ 3.1 Å. The peaks generally ascribed as being FSDPs are usually present at $Q \sim 1$ Å^{-1}, corresponding to density fluctuations on a significantly longer length-scale (of the order of ~ 6.2 Å), that is, well beyond the natural length-scales associated with simple atom packing and generally termed intermediate- (or medium-) ranged order (IRO or MRO).[10,74] As a result of the inherent complexity, a void analysis such as that described above is often employed. In even simple mixed-atom systems, such as $ZnCl_2$ or $GeSe_2$, the nature of the IRO is further complicated by the observation that the density fluctuations on the extended length-scale may be associated with one sublattice only, whereas the respective roles of simple density and concentration fluctuations may be complex.[75] In the single atom system, however, these fluctuations are simply the result of density fluctuations on longer length-scales than that imposed by the atom radii (packing effects), and hence both the atomic and void structures should be relatively simple to interpret. Zaug et al.[76] considered the behavior of the FSDP in amorphous phosphorus as a function of pressure. In that case, the ambient pressure feature appears at $Q \sim 1.08$ Å^{-1} and, as a result, can be classified as a true FSDP. Furthermore, the FSDP shows relatively little change in position on pressurization (the peak does not behave like a "normal" principal peak as would the first peak in a pseudoclose-packed disordered network). Analysis of the void structure shows a systematic reduction in the free space as the pressure is increased, consistent with intermediate-ranged structural changes. In the present work, both the LDA and HDA configurations for a-Si are characterized by networks in which the first peak in both $S(Q)$ and $S_{VV}(Q)$ mirror each other. The LDA configurations are characterized by near-ideal linked tetrahedra, while the HDA phase contains significant numbers of five-coordinate sites, which effectively partially fill the voids (hence the mirroring shifts of both $S(Q)$ and $S_{VV}(Q)$ to higher Q, that is, the length-scales associated with the first peaks in these functions is reduced). As a result, the FDPs in both the atom and void structure behave "normally" and are, therefore, best considered as principal peaks rather than FSDPs.

■ CONCLUSIONS

Our low-frequency Raman data obtained for amorphous Si during compression in the DAC along with calculations of the temperature-dependent heat capacity and MD simulations confirm that a-Si does not exhibit boson peak behavior. There are no anomalous excitations in the low frequency regime that can be assigned to nanoscale mechanical or dynamical heterogeneities in the amorphous structure. Instead the low frequency excitations correspond to the VDOS derived from acoustic phonons propagating within the amorphous structure as found in corresponding crystalline materials. The TA band observed by low-frequency Raman scattering in the LDA polyamorph shifts to lower wavenumber as pressure is increased, analogous to observations made for crystalline diamond- and clathrate-structured polymorphs. A distinct low-frequency band is observed to persist above the LDA−HDA polyamorphic transition at 12−15 GPa, in agreement with our MD simulations and previous ab initio MD results. This band is narrower than that observed for the LDA form, and it shifts to lower wavenumber with increasing pressure. The similarity of the present experimental and theoretical data with that of the ab initio MD simulations of Morishita also strongly suggests that the structure of experimentally observed HDA-Si is that of a highly defective (five-coordinate) distorted tetrahedral network.

The present study supports previous observations that any "excess" of low-frequency vibrational states is less marked in the glassy state than in the corresponding crystal and thus indicates the absence of a boson feature, or at least the existence of only a very weak one. Models proposed for the appearance of this feature include the presence of nanoscale mechanical heterogeneities that promote the localization of acoustic modes. In addition, excitations may also be promoted at the interfaces between elastically "strong" and "weak" domains.[6,7] The existence of the boson peak has also been correlated with the FSDP and nanoscale density fluctuations. In a-Si, however, the density fluctuations associated with the FDP occur on too short a length-scale to support significant numbers of such modes.

■ ACKNOWLEDGMENT

■ REFERENCES

(1) Laaziri, K.; Kycia, S.; Roorda, S.; et al. *Phys. Rev. Lett.* **1999**, *82*, 3460.
(2) Zink, B. L.; Pietri, R.; Hellman, F. *Phys. Rev. Lett.* **2006**, *96*, 055902.
(3) Zeller, R. C.; Pohl, R. O. *Phys. Rev. B* **1971**, *4*, 2029.
(4) Phillips, W. A. *J. Low Temp. Phys.* **1972**, *7*, 351.
(5) Phillips, W. A. *Rep. Prog. Phys.* **1987**, *50*, 1657.
(6) Duval, E.; Mermet, A.; Saviot, L. *Phys. Rev. B* **2007**, *75*, 024201.
(7) Shintani, H.; Tanaka, H. *Nat. Mater.* **2008**, *7*, 870.
(8) Elliott, S. R. *Europhys. Lett.* **1992**, *19*, 201.
(9) Sokolov, A. P.; Kisliuk, A.; Soltwisch, M.; et al. *Phys. Rev. Lett.* **1992**, *69*, 1540.
(10) Salmon, P. S. *Proc. R. Soc. London* **1994**, *445*, 351.
(11) Angell, C. A.; Ngai, K. L.; McKenna, G. B.; et al. *J. Appl. Phys.* **2000**, *88*, 3113.
(12) Angell, C. A. *J. Phys.: Condens. Matter* **2000**, *12*, 6463.
(13) Angell, C. A.; Bressel, R. D.; Hemmati, M.; et al. *Phys. Chem. Chem. Phys.* **2000**, *2*, 1559.
(14) Benmore, C. J.; Hart, R. T.; Mei, Q.; et al. *Phys. Rev. B* **2005**, *72*, 132201.
(15) Tang, X.; Dong, J. J.; Hutchins, P.; et al. *Phys. Rev. B* **2006**, *74*, 014109.
(16) Ponyatovsky, E. G.; Barkalov, O. I. *Mater. Sci. Rep.* **1992**, *8*, 147.
(17) Poole, P. H.; Grande, T.; Angell, C. A.; et al. *Science* **1997**, *275*, 322.
(18) Mishima, O.; Stanley, H. E. *Nature* **1998**, *396*, 329.
(19) Tanaka, H. *Phys. Rev. E* **2000**, *62*, 6968.
(20) Yarger, J. L.; Wolf, G. H. *Science* **2004**, *306*, 820.
(21) McMillan, P. F. *J. Mater. Chem.* **2004**, *14*, 1506.
(22) Morishita, T. *J. Chem. Phys.* **2009**, *130*, 194709.
(23) McMillan, P. F.; Wilson, M.; Daisenberger, D.; et al. *Nat. Mater.* **2005**, *4*, 680.
(24) Aptekar, L. I. *Sov. Phys. Dokl.* **1979**, *24*, 993.
(25) Sastry, S.; Angell, C. A. *Nat. Mater.* **2003**, *2*, 739.
(26) Jakse, N.; Pasturel, A. *J. Chem. Phys.* **2008**, *129*, 104503.
(27) Daisenberger, D.; Wilson, M.; McMillan, P. F.; et al. *Phys. Rev. B* **2007**, *75*, 224118.
(28) Eggert, J. H.; Weck, G.; Loubeyre, P.; et al. *Phys. Rev. B.* **2002**, *65*, 174105.
(29) McMillan, P. F.; Gryko, J.; Bull, C.; et al. *J. Solid State Chem.* **2005**, *178*, 937.
(30) Deschamps, T.; Martinet, C.; Neuville, D. R.; et al. *J. Non-Cryst. Solids* **2009**, *355*, 2422.
(31) Champagnon, B.; Wondraczek, L.; Deschamps, T. *J. Non-Cryst. Solids* **2009**, *355*, 712.
(32) Galeener, F. L.; Leadbetter, A. J.; Stringfellow, M. W. *Phys. Rev. B* **1983**, *27*, 1052.
(33) Li, F.; Lannin, J. S. *Phys. Rev. B* **1989**, *39*, 6220.
(34) Zwick, A.; Carles, R. *Phys. Rev. B* **1993**, *48*, 6024.
(35) Nakhmanson, S. M.; Drabold, D. A. *Phys. Rev. B* **2000**, *61*, 5376.
(36) Smith, V. H.; Thakkar, A. J.; Chapman, D. C. *Acta Crystallogr.* **1975**, *A31*, 391.
(37) Krogh-Moe, J. *Acta Crystallogr.* **1956**, *9*, 951.
(38) Norman, N. *Acta Crystallogr.* **1957**, *10*, 370.
(39) Waasmaier, D.; Kirfel, A. *Acta Crystallogr.* **1995**, *A51*, 416.
(40) Hubbell, J. H.; Veigele, W. J.; Briggs, E. A.; et al. *J. Phys. Chem. Ref. Data* **1975**, *4*, 471.
(41) NIST Physical Measurement Laboratory Page. http://physics.nist.gov/PhysRefData/XrayMassCoef/cover.html.
(42) Kaplow, R.; Strong, S. L.; Averbach, B. L. *Phys. Rev.* **1965**, *138*, A1336.
(43) Laaziri, K.; Kycia, S.; Roorda, S.; et al. *Phys. Rev. B* **1999**, *60*, 13520.
(44) Stillinger, F. H.; Weber, T. A. *Phys. Rev. B* **1985**, *31*, 5262.
(45) Cook, S. J.; Clancy, P. *Phys. Rev. B* **1993**, *47*, 7686.
(46) Luedtke, W. D.; Landman, U. *Phys. Rev. B* **1989**, *40*, 1164.
(47) Justo, J. F.; Bazant, M. Z.; Kaxiras, E.; et al. *Phys. Rev. B* **1998**, *58*, 2539.
(48) Luedtke, W. D.; Landman, U. *Phys. Rev. B* **1988**, *37*, 4656.
(49) Custer, J. S.; Thompson, M. O.; Jacobson, D. C.; et al. *Appl. Phys. Lett.* **1994**, *64*, 437.
(50) Hoover, W. G. *Phys. Rev. A* **1985**, *31*, 1695.
(51) Martyna, G. J.; Tobias, D. J.; Klein, M. L. *J. Chem. Phys.* **1994**, *101*, 4177.
(52) Marinov, M.; Zotov, N. *Phys. Rev. B* **1997**, *55*, 2938.
(53) Vink, R. L. C.; Barkema, G. T.; van der Weg, W. F. *Phys. Rev. B* **2001**, *63*, 115210.
(54) Alben, R.; Weaire, D.; Smith, J. E.; et al. *Phys. Rev. B* **1975**, *11*, 2271.
(55) Bernal, J. D. *Proc. R. Soc. A* **1964**, *280*, 299.
(56) Finney, J. L. *Proc. R. Soc. A* **1970**, *319*, 495.

(57) Naberukhin, Y. I.; Voloshin, V. P.; Medvedev, N. N. *Mol. Phys.* **1991**, *73*, 917.

(58) Ivanda, M.; Gamulin, O.; Kiefer, W. *J. Mol. Struct.* **1999**, *480−481*, 651.

(59) Kamitakahara, W. A.; Soukoulis, C. M.; Shanks, H. R.; et al. *Phys. Rev. B* **1987**, *36*, 6539.

(60) Smith, J. E.; Brodsky, M. H.; Crowder, B. L.; et al. *Phys. Rev. Lett.* **1971**, *26*, 642.

(61) Maley, N.; Beeman, D.; Lannin, J. S. *Phys. Rev. B* **1988**, *38*, 10611.

(62) Kamitakahara, W. A.; Shanks, H. R.; McClelland, J. F.; et al. *Phys. Rev. Lett.* **1984**, *52*, 644.

(63) Vink, R. L. C.; Barkema, G. T.; van der Weg, W. F.; et al. *J. Non-Cryst. Solids* **2001**, *282*, 248.

(64) Deb, S. K.; Wilding, M.; Somayazulu, M.; et al. *Nature* **2001**, *414*, 528.

(65) Wu, B. R. *Chin. J. Phys.* **2006**, *44*, 454.

(66) Klotz, S.; Besson, J. M.; Braden, M.; et al. *Phys. Rev. Lett.* **1997**, *79*, 1313.

(67) McMillan, P. F.; Shebanova, O.; Daisenberger, D.; et al. *Phase Transitions* **2007**, *80*, 1003.

(68) Dong, J. J.; Sankey, O. F.; Kern, G. *Phys. Rev. B* **1999**, *60*, 950.

(69) Guyot, Y.; Grosvalet, L.; Champagnon, B.; et al. *Phys. Rev. B* **1999**, *60*, 14507.

(70) Ramachandran, G. K.; McMillan, P. F.; Deb, S. K.; et al. *J. Phys.: Condens. Matter* **2000**, *12*, 4013.

(71) Wilson, M.; Madden, P. A. *Phys. Rev. Lett.* **1998**, *80*, 532.

(72) Durandurdu, M.; Drabold, D. A. *Phys. Rev. B* **2001**, *64*, 014101.

(73) Durandurdu, M.; Drabold, D. A. *Phys. Rev. B* **2002**, *66*, 155205.

(74) Elliott, S. R. *Nature* **1991**, *354*, 445.

(75) Salmon, P. S.; Martin, R. A.; Mason, P. E.; et al. *Nature* **2005**, *435*, 75.

(76) Zaug, J. M.; Soper, A. K.; Clark, S. M. *Nat. Mater.* **2008**, *7*, 890.